# NUMERICAL RESEARCH OF THE NACELLE STRAKE ON A CIVIL JET

**Wensheng Zhang*, Haixin Chen**, Yufei Zhang**， Song Fu****
**Yingchun Chen***, Yalin Li***, Tao Zhou*****
***Beijing Aeronautical Science & Technology Research Institute, Beijing 102211, China***
**** School of Aerospace, Tsinghua University, Beijing 100084, China***
*****Shanghai Aircraft Design & Research Institute, Shanghai, 200236, China***
*zhangws09@mails.tsinghua.edu.cn;chenhaixin@tsinghua.edu.cn;zhangyufei@tsinghua.edu.cn;*
*fs-dem@tsinghua.edu.cn;chenyingchun@comac.cc;liyalin@comac.cc;zhoutao@comac.cc*

## Abstract

*The present paper is focused on the mechanism investigation and parameter analysis of the nacelle strake on the high-lift configuration of a civil jet. Different nacelle strake configurations are numerically simulated and compared. The influences of the installation parameters of the nacelle strake are studied. Flow field analysis is carried out. The flow control mechanisms are discussed.*

## 1 Introduction

The success of aircraft design depends on the accurate performance analysis and appropriate setting of parameters. High-lift configuration design is an important part of the wing design, especially civil transport wing design. The primary function of the high-lift system is to shorten the distance of taking-off and landing; From the safety point, high-lift system should be able to generate enough lift to guarantee a lower enough stall speed for the aircraft; Meredith et al. [1] discussed the importance of high-lift system: an increase in maximum lift coefficient by 1.0% get an increase in payload by 22 passengers or 4400lb payload for a specified landing approach speed.

For modern civil jets, when under-wing mounted, the engine nacelles are tightly coupled with the wing. The nowadays large by-pass ratio power plant makes the nacelle have great adverse influence on the wing’s performances, especially when the high-lift devices are deployed. The premature massive flow separation on main-wing caused by the nacelle will decrease both the maximum lift coefficient and the stall angle, make the high lift configuration not able to reach the desired performance [2,3]. In order to alleviate the nacelle’s adverse influence, recover the maximum lift coefficient and the stall angle, strake (chine) is designed and installed on appropriate position on the nacelle[3,4]. Nowadays, the design of nacelle strake becomes an important issue in the civil aircraft design. Europe started the EUROLIFT project on 2000[5]. Numerical study and wind tunnel test about high-lift configuration were carried out. EUROLIFT II project was started on 2004[6]. In this continuing project, the stall behavior of high-lift configuration became one of the most important research object. The influence of the nacelle and strake are paid much attention in this project. Numerical simulations and tunnel test results show that strake can effectively delay the nacelle caused stall and increase the usable angle of attack.

Although the Computational Fluid Dynamics (CFD) and computer hardware have got great advancement in the past years, numerical simulation of the flow around high-lift configuration is still challenging. The difficulties come from the complicated geometry and relevant complicated flow structure of high-lift configuration. The geometry discontinuities at slat and flap ends cause great difficulties to structural grid generation. Due to the complicated geometry, there are various complicated flow phenomenon in high-lift configuration, such as boundary

layer separation, laminar/turbulent transition, wakes, shock/boundary layer interaction and unsteady flow, these flow phenomenon also interact with each other[7]. When the strake is incorporated, the grid generation will become even more difficult. The flow field will also become much more complicated. The necessity of accurately predicting the strake generated vortex's strength and trajectory raise great difficulties to the qualities of both the grid and numerical methods.

The present paper is focused on the study of the mechanisms of the nacelle strake. Parametric studies of the nacelle strake's geometry and location are also carried out. The high-lift configuration investigated in this research is a very complex one. It is made up of fuselage, main-wing, winglet, slat, flap, flap rack fairings, horizontal tail and vertical tail, as well as the nacelle, pylon, and strake. Before doing research on such a realistic configuration, the CFD solver and grid are first verified by standard high-lift test case with wind tunnel data.

## 2 Validation of the CFD Solver

### 2.1 NSAWET code

The in-house CFD code named NSAWET (Navier-Stokes Analysis based on Window Embedment Technology) [9,16] is employed for the numerical simulations. It's a structural grid RANS solver based on cell-centered finite volume method. Multiple spatial and time advancing schemes and several widely used turbulence models are integrated in the code.

According to the past experiences of using NSAWET[17,18], in the present numerical simulation, Roe's FDS spatial discretization and LU-SGS time stepping, as well as SST turbulence model are selected.

### 2.2 Validation on High-lift Configuration

The flow solver is first validated by the standard model of the 1st AIAA High-Lift Prediction Workshop [8].

In order to advance the understanding of the high-lift flow physics and enhance the CFD's capability for high-lift aerodynamic design and optimization, the 1st AIAA High-Lift Prediction Workshop was held in Chicago in 2010. The workshop uses the NASA Trap Wing high-lift model, which is made up of fuselage and full span slat/flap, as shown in Fig. 1. Configurations with different flap deflection angles, designated as Config1 and Config8 are studied in the workshop. In the present paper, only Config1 is simulated. The deflection angles of the slat and the flap are 30 degree and 25 degree, respectively. The experimental Mach number is 0.2 and the Reynolds number based on mean aerodynamic chord is 4.3 million.

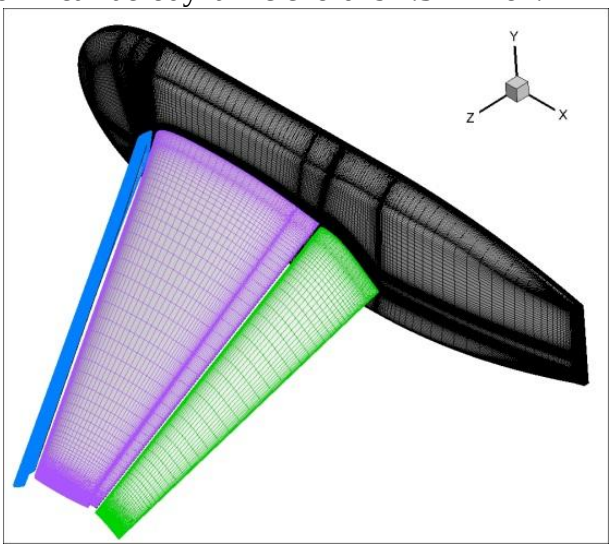


Fig. 1. Surface grid of NASA Trap Wing high-lift model (Config1)

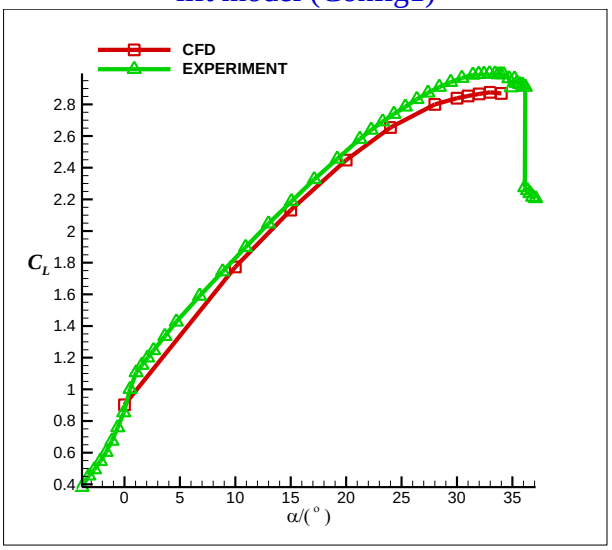


Fig. 2. Lift coefficient comparison between results of CFD and wind tunnel experiment

Multi-block grid is generated by ICEM-CFD. The surface grid is showed in Fig. 1. The total grid nodes are about 30 million. To ensure

that the $Y^+$ is below 1, the first grid spacing in normal direction of the wall is set to 0.00013. Such a criteria is given by the workshop gridding guidelines [10].

Fig.2 shows lift coefficient comparison between the results of NSAWET and the wind tunnel experimental data. In the whole range of angle of attack (AoA), from 0 degree to 34 degree, the computed lift coefficients are slightly smaller than the test data. The difference on maximum lift coefficient between the CFD results and test data is 3.99%. The maximum error in the linear range is 3%. The computed stall AoA is 33 degree which is nearly identical to the test data.

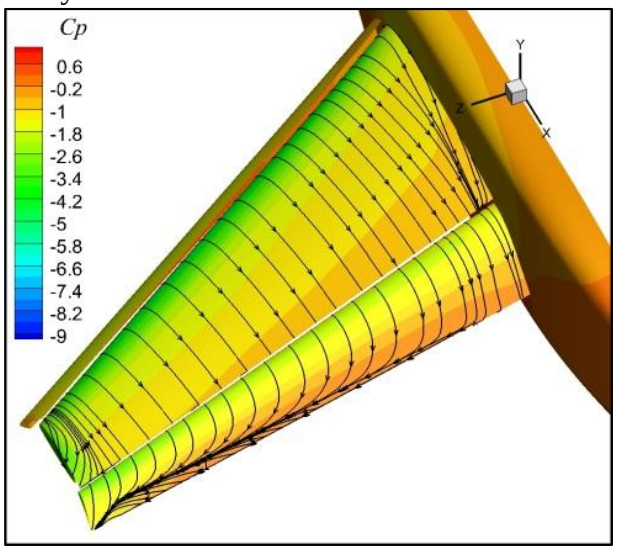


Fig. 3. Surface pressure coefficient contour and surface streamlines (AoA=15 degree)

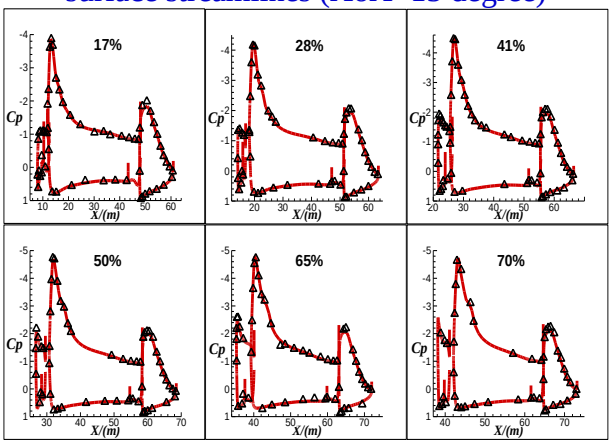


Fig. 4. Cp distribution comparison between results of CFD and wind tunnel test (AoA=15 degree)

As showed in Fig. 3, there is obvious flow separation at the wing tip of the main-wing, also at the flap trailing edge covering a large span-wise extent. The pressure coefficient distribution (*Cp*) comparison is shown in Fig. 4. The computed pressure coefficient distributions on profiles located from 17% to 70% semi-span are in very good agreement with the test data, even there is flow separation.

From above, the accuracy of NSAWET can be concluded to be satisfying for the simulation of high-lift flow.

## 3 Numerical Analysis

### 3.1 Grid Generation

Because of the extremely complicated geometry, unstructured grid and overlapping grid are widely used in the numerical simulation of high-lift configurations [11,12]. The conclusions from EUROLIFT II project show that using unstructured grid with reliable flow solver can get a good accuracy of the high-lift flow field, while large number of grid nodes is needed. The project also concluded that the overlapping grid techniques for high lift flows show good results but some grid dependencies are observed[12].

In order to better simulate boundary layer flow and boundary layer/vortex interaction, point-to-point structural grid is applied in the present numerical simulation. High quality multi-block grid is successfully generated for the realistic high-lift configuration, which consists of fuselage, main-wing, winglet, slat, flap, flap track fairings, horizontal tail and vertical tail, as well as the nacelle, pylon, and strake. The geometry and surface grid is shown in Fig. 5(a), (b), (c), and the spatial grid is shown in Fig. 5(d), (e). According to the earlier study, it was found that the thickness of nacelle strake has little effect on the flow control performances. Hence the strake is simplified into a zero-thickness plate. In order to better resolve the boundary layer and vortices arising from the end of flap/slat/main-wing with as few grid nodes as possible, “O-type” grid is applied surrounding the wall. 33 layers of grid are used and the first grid spacing is set to ensure the $Y^+$ is less than 1. The grid stretching ratio is 1.2 near the wall and 1.5 in far field. The total number of grid nodes is 33 million. The grid

topology and clustering is carefully adjusted to guarantee the resolution of key flow structures. A baseline grid is first generated. For different strake configurations, only local changes to the grid are made. This makes it's possible to resolve and compare the effects caused by different strakes.

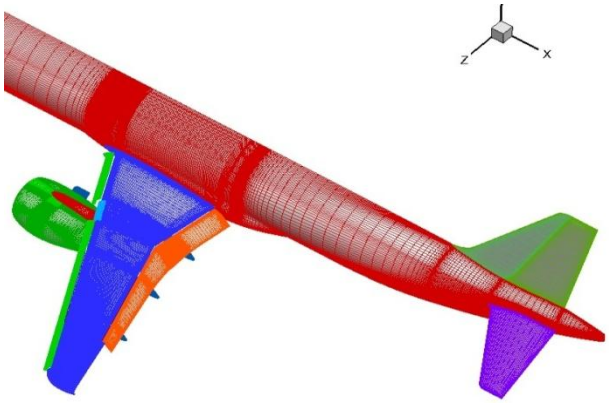

(a)

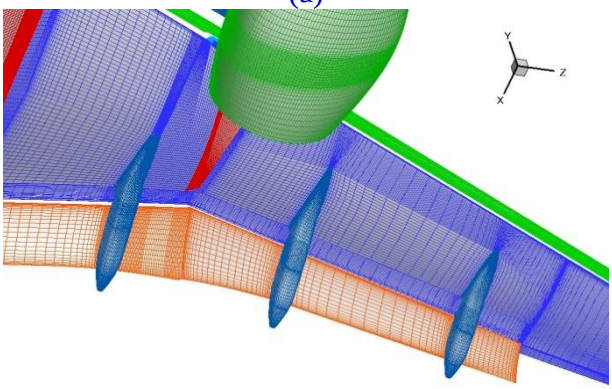

(b)

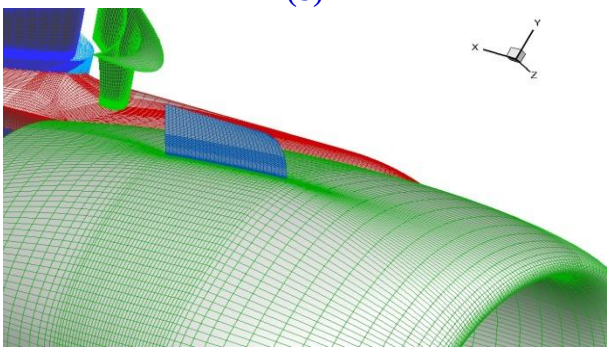

(c)

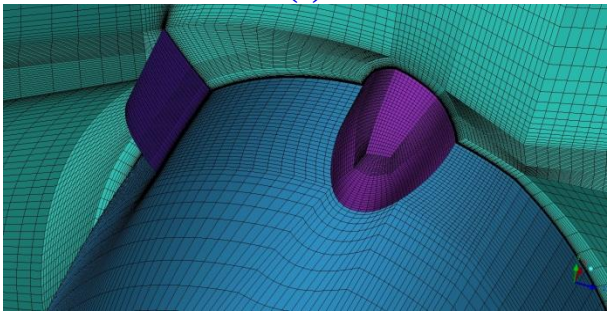

(d)

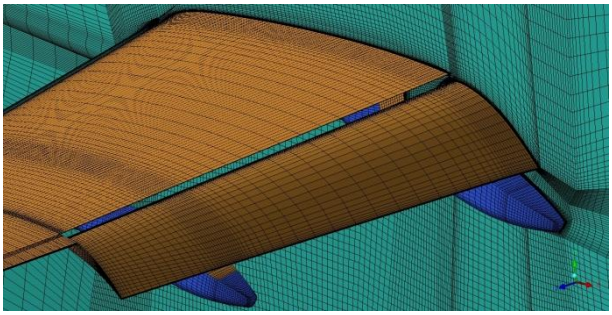

(e)

Fig. 5. Surface grid and spatial grid of high-lift configuration

### 3.2 Flow Control Mechanism Analysis

Before parametrically study the nacelle strake, flow fields with and without strake are firstly compared to analyze the mechanism of the strake's flow control effects.

In Fig. 6, total pressure coefficient ($Cp_0$) contour on spatial slices are compared between configurations with and without strake. The $Cp_0$ is defined as:

$$Cp_0 = 2(P_0 - P_{0\infty}) / (\rho V_\infty^2) \qquad (1)$$

As shown in Fig. 6(a), for the configuration without strake (left), large area of low energy flow above the main-wing is detected at a close-to-stall AoA (12 °). It is obvious that such a low energy area is caused by the nacelle's blockage to the flow passing the upper surface of wing at high AoA. This low energy area will lead to premature flow separation when the AoA further increases. For the configuration with strake (right), flow visualization shows that the massive low energy area caused by the nacelle has been eliminated by the vortex generated by the strake. The strake vortex goes through the low energy area and brings surrounding high total pressure flow into this area. The flow is therefore reenergized. In Fig. 6(b), the configuration without the strake obviously has stalled. However with the strake, as is shown on the right, the separation is suppressed and the stall is delayed.

Fig.7 shows the $Cp$ distribution of the high-lift configurations with and without strake at the 35% span-wise station of the wing, which is right above the nacelle. It indicates that the flow separation on the upper surface of the

main-wing and the flap is both mitigated when the strake is presented. With these nacelle strake effects, the lift on the main-wing and flap is greatly recovered. The maximum lift coefficient and stall AoA can both be greatly improved.

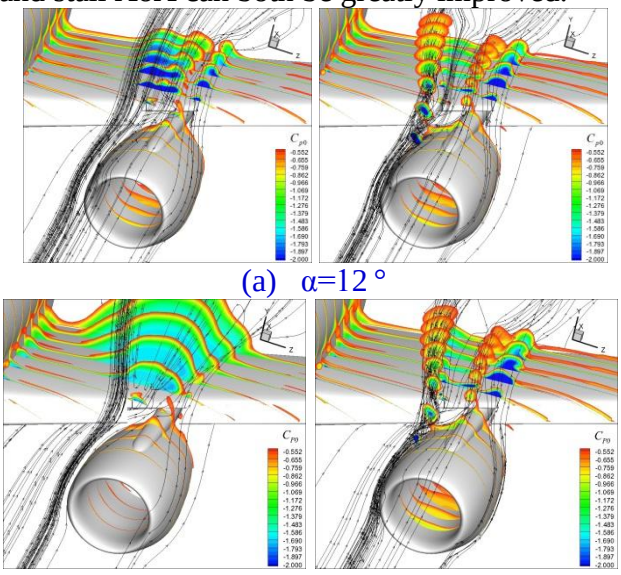

(a) α=12 °

(b) α=14 °

Without strake With strake

Fig. 6 Total pressure coefficient contour comparison between models with strake and without strake
（Ma=0.2,Re=2.0E7）

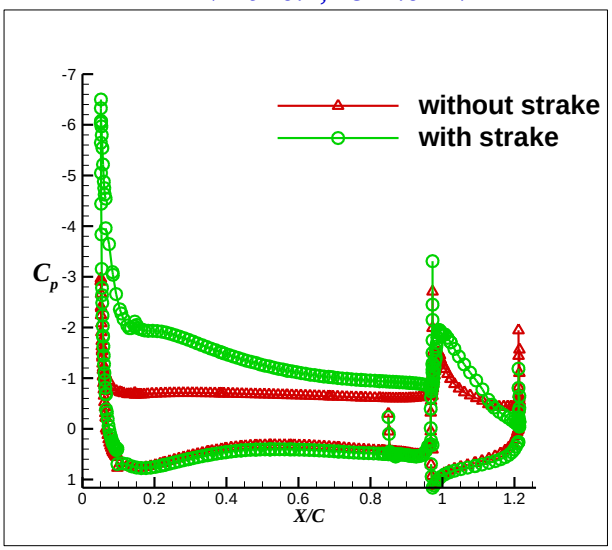


Fig. 7. Cp distribution comparisons between models with and without strake at the section of 35% span-wise
（Ma=0.2,Re=2.0E7, α=14 °）

The flow control mechanism of the nacelle strake can be concluded as: generating vortex which goes through the separation area caused by the nacelle, entrain flow with high kinetic energy into that area to delay the flow separation. Therefore the strength and the trajectory of the strake vortex are the two key factors determine the strake effects.

### 3.3 Parametric investigation of nacelle strake

The parameter design of nacelle strake have been carried out by using tunnel experiment in JAXA of Japan[13-15]. In the present paper, parametric studies of the strake's geometry and installation by CFD are conducted. The influence of the area and the axial locations of the strake on the nacelle are tested. The axial location is defined as the distance between the trailing edges of nacelle and strake, normalized by the length of nacelle.

Fig. 8 shows four strake configurations designed in the paper. The strake 1, strake 2 and strake 4 have the same area, while their axial locations are different. They are at 39%, 30% and 64% respectively. The strake 2 and strake 3 have the same axial location. The area of the strake 3 is two third of that of the strake 2. The strake's azimuth location on the nacelle is not considered in the paper.

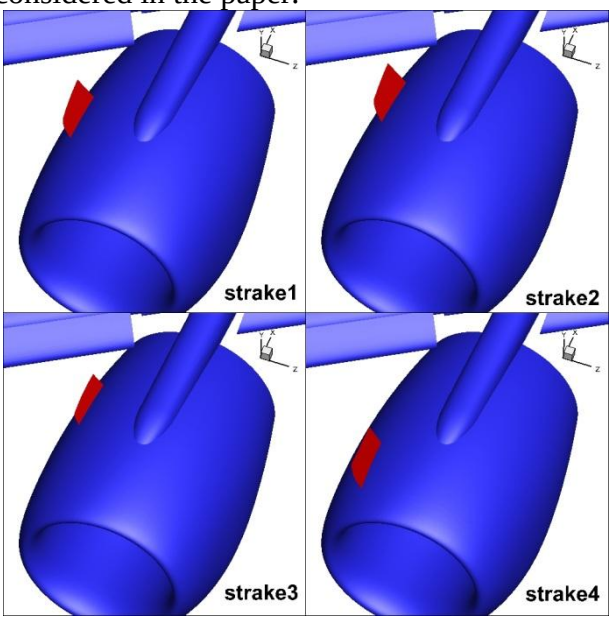


Fig. 8. Four configurations of nacelle strake

In Fig. 9, lift coefficient curves of the four strake configurations are compared with that of the configuration without strake. The strake effect can be seen from the lift comparison between configurations with and without strake. When the "best" strake, say strake2, in this

paper is installed, the maximum lift coefficient is increased by more than 0.3 and the stall AoA is increased by 3 degrees. The linearity of the lift curve is also improved. For strake 2, strake 1 and strake 4 sequentially, the strake's axial location is going more and more far away from the nacelle's trailing edge. The maximum lift coefficient is decreasing. Compared with Strake 2, the area of Strake 3 is smaller. There is little difference between their lift coefficients before the stall angle. However difference is shown after their stall AoA: the smaller strake produced an abrupt drop of lift coefficient. From these phenomena, the strake's axial location is found to be the key factor that determines the stall-delay capability. Within the range of the axial locations computed in the paper, the closer the strake to the trailing edge, the higher the maximum lift coefficient can be.

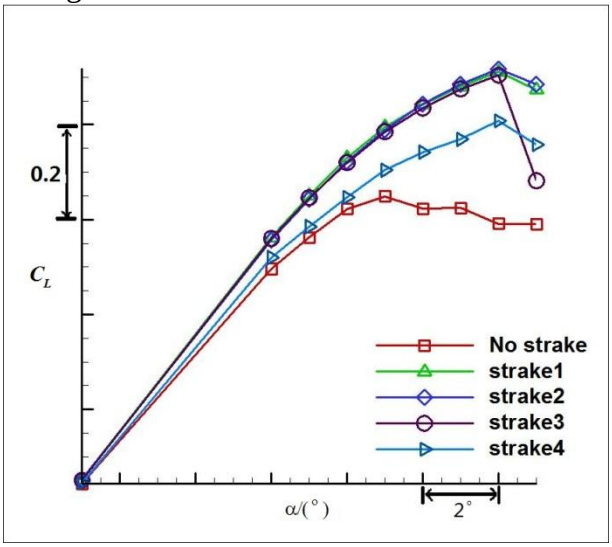


Fig. 9. Lift coefficient curves of different configurations (Ma=0.2，Re=2.0E7, , α=14 °)

Fig. 10 shows the spatial stagnation pressure coefficient contour and stream lines, compared among the four configurations at AoA=16 °. Strake 1, strake2 and strake 3 eliminate the flow separation caused by nacelle effectively, while the flow control effect of strake 4 is not as good. It can be seen from the figure that the vortex generated by strake 2 is the strongest and the one by strake 4 is the weakest. From Fig. 9, it is known that the flow control effect of strake 2 is the best and strake 4 is the worst. The strength of the strake vortex should be a key factor that affects the strake's stall-delay effect.

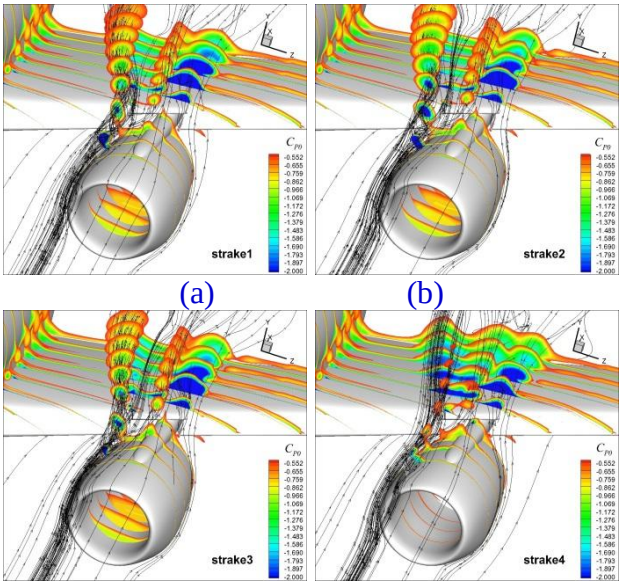


Fig. 10. Total pressure coefficient contour comparison between different configurations (Ma=0.2, Re=2.0E7, α=16 °)

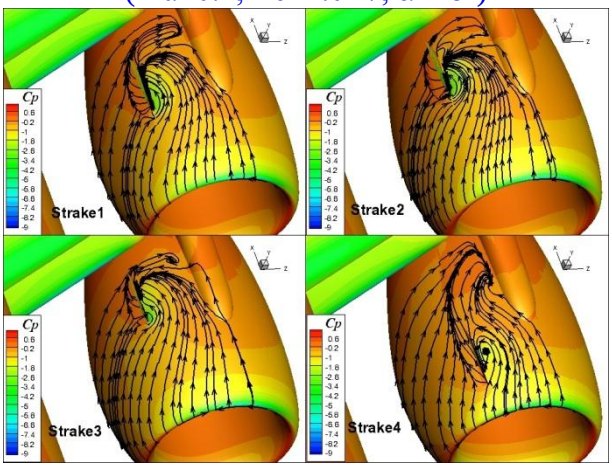


Fig. 11. Surface streamlines around different strakes (Ma=0.2, Re=2.0E7, α=16 °)

In order to get a full understanding of the relationship between the strake's vortex strength and its installation, local flow fields are carefully studied. From the surface streamlines around different strakes shown in Fig. 11, it is found that the velocity vector component normal to the strake, or the circumferential component of the velocity, decreases when the distance between the strake and the nacelle's trailing edge increases. This trend of the strake's local angle of attack determines the strength of strake vortex. Therefore, as can be found in Fig. 10, the vortex generated by strake 2 is the strongest and the vortex generated by strake 4 is the weakest.

From the above discussion, in order to improve the strake's effect of stall delay, it should be placed at a location where it will have a large local angle of attack. It can be found that, on the upper side of the nacelle, from the leading edge to the trailing edge, the circumferential component of the velocity is increasing. Such a trend exists no matter the strake is present or not. Therefore the streamlines on a clean nacelle without strake can help to find an optimum location for the strake.

## 4 Conclusion

Through a series of numerical simulations for the high-lift configuration with inboard nacelle strakes and the analysis of the results, the influences of the size and installation parameters of the nacelle strake, as well as its flow control mechanism are found.

(1) The vortex generated by the strake eliminates flow separation over the upper surface of the wing right behind the nacelle, and then recovers the lift on both the main-wing and the flap. As a result, the stall is delayed and the maximum lift is improved. The best practice design of the strake from the research can improve the maximum lift coefficient by more than 0.3 and the stall angle by 3 degrees.

(2) The axial location on the nacelle determines the circumferential component of the flow and hence determine the strake's local AoA. The local AoA is a key factor of the strength of the strake vortex, when the strake's azimuth location is set. The strength of strake vortex is a key factor of the strake's stall-delay effect.

(3) The azimuth location and deflection angle of the strake should be carefully studied to find how they can affect the strength and trajectory of the strake vortex.

## Acknowledgement

The numerical research is carried out under the project 10972120 supported by National Natural Science Foundation of China.

## References

[1] Meredith P. T. Viscous Phenomena Affecting High-Lift Systems and Suggestions for Future CFD Development. *High-Lift Systems Aerodynamics*. AGARD, CP 315, Sep. 1993, pp. 19-1~19-8.

[2] R. Rudnik. Stall Behaviour of the EUROLIFT High Lift Configurations. *46th AIAA Aerospace Sciences Meeting and Exhibit*. AIAA Paper 2008-836, Reno, Nevada, January 2008.

[3] Harald Quix, Matthias Schulz and Jürgen Quest, et. al. Low Speed High Lift Validation Tests within the European Project EUROLIFT II. *25th AIAA Applied Aerodynamics Conference*. AIAA Paper 2007-4298, Miami, FL, June 2007.

[4] H. Frhr. v. Geyr, N. Schade, J.W. v. d. Burg, et. al. CFD Prediction of Maximum Lift Effects on Realistic High Lift Commercial Aircraft Configurations within the European project EUROLIFT II . *25th AIAA Applied Aerodynamics Conference*. AIAA Paper 2007-4299, Miami, FL, June 2007.

[5] Heinz Hansen, Peter Thiede, Frederic Moens, et. al. Overview about the European high lift research programme EUROLIFT. *42nd AIAA Aerospace Sciences Meeting and Exhibit*. AIAA Paper 2004-767, Reno, Nevada, January 2004.

[6] R. Rudnik, H. Frhr. v. Geyr. The European High Lift Project EUROLIFT II –Objectives, Approach, and Structure. *25th AIAA Applied Aerodynamics Conference*. AIAA Paper 2007-4296, Miami, FL, June 2007.

[7] Christopher L. Rumsey, Susan X. Ying. Prediction of high lift: review of present CFD capability. Progress in Aerospace Sciences. Vol. 38, pp 145-180, 2002.

[8] Jeffrey P. Slotnick, Judith A. Hannon, Mark Chaffin. Overview of the First AIAA CFD High Lift Prediction Workshop. *49th AIAA Aerospace Sciences Meeting including the New Horizons Forum and Aerospace Exposition*. AIAA Paper 2011-862, Orlando, Florida, January 2011.

[9] HaiXin Chen, Song Fu, FengWei Li. Navier–Stokes Simulations for Transport Aircraft Wing/Body High-Lift Configurations, *JOURNAL OF AIRCRAFT*, Vol. 40, No. 5,pp883-890, 2003.

[10] 1st AIAA CFD High Lift Prediction Workshop Gridding Guidelines, http://hiliftpw.larc.nasa.gov.

[11] Niko F. Bier, David Rohlmann, Ralf Rudnik. Numerical Maximum Lift Predictions of a Realistic Commercial Aircraft in Landing Configuration. *50th AIAA Aerospace Sciences Meeting including the New Horizons Forum and Aerospace Exposition*. AIAA Paper 2012-279, Nashville, Tennessee, January 2012.

[12] Peter Eliasson, Pietro Catalano, Marie-Claire Le Pape, et al. Improved CFD Predictions for High Lift Flows in the European Project EUROLIFT II. *25th AIAA Applied Aerodynamics Conference*. AIAA Paper 2007-4303, Miami, FL, June 2007.

[13] Masahiro Kanazaki, Yuzuru Yokokawa，Mitsuhiro Murayama，et al., Efficient Design Exploration of Nacelle Chine Installation in Wind Tunnel Testing. *46th AIAA Aerospace Sciences Meeting and Exhibit.* AIAA Paper 2008-155, Reno, Nevada, January 2008.

[14] Yuzuru Yokokawa, Mitsuhiro Murayama, Masahiro Kanazaki, et al., Investigation and Improvement of High-lift Aerodynamic Performances in Lowspeed Wind Tunnel Testing. 46th AIAA Aerospace Sciences Meeting and Exhibit. AIAA Paper 2008-350, Reno, Nevada, January 2008.

[15] Yuzuru YOKOKAWA, Mitsuhiro MURAYAMA, Hiro-shi UCHIDA, et al., Aerodynamic Influence of a Half-Span Model Installation for High-Lift Configuration Experiment. *48th AIAA Aerospace Sciences Meeting Including the New Horizons Forum and Aerospace Exposition*. AIAA Paper 2010-684, Orlando, Florida, January 2010.

[16] Zhang Y., Chen H., Fu S., Improvement to Patched Grid Technique with High-Order Conservative Remapping Method, *JOURNAL OF AIRCRAFT*, Vol. 48, No. 3, pp. 884-893,2011.

[17] Zhang Yufei, Chen Haixin, Zhang Wensheng, et al., Wing/engine integrated optimization based on Navier-Stokes equations. *50th AIAA Aerospace Sciences Meeting including the New Horizons Forum and Aerospace Exposition*. AIAA Paper 2012-1046, Nashville, Tennessee, January 2012.

[18] Zhang Yufei, Chen Haixin, Fu Song. A Karman-Vortex Generator for Passive Separation Control in a Conical Diffuser. *SCIENCE CHINA Physics, Mechanics & Astronomy*, Vol.55, No. 5, pp. 828-836, 2012.

## Copyright Statement